The 2014 M_w 6.1 South Napa Earthquake: A Unilateral Rupture with Shallow Asperity and Rapid Afterslip

by Shengji Wei, Sylvain Barbot, Robert Graves, James J. Lienkaemper, Teng Wang, Kenneth Hudnut, Yuning Fu, and Don Helmberger

Online Material: Figures of waveform and peak ground velocity fit, sensitivity for dip of segment S1, horizontal Global Positioning System and Interferometric Synthetic Aperture Radar offsets, and digital slip model.

INTRODUCTION

The M_w 6.1 South Napa earthquake occurred near Napa, California, on 24 August 2014 at 10:20:44.03 (UTC) and was the largest inland earthquake in northern California since the 1989 M_w 6.9 Loma Prieta earthquake. The first report of the earthquake from the Northern California Earthquake Data Center (NCEDC) indicates a hypocentral depth of 11.0 km with longitude and latitude of (122.3105° W, 38.217° N). Surface rupture was documented by field observations and Light Detection and Ranging (LiDAR) imaging (Brooks *et al.*, 2014; Hudnut *et al.*, 2014; Brocher *et al.*, 2015), with about 12 km of continuous rupture starting near the epicenter and extending to the northwest. The southern part of the rupture is relatively straight, but the strike changes by about 15° at the northern end over a 6 km segment. The peak dextral offset was observed near the Buhman residence with right-lateral motion of 46 cm, near the location where the strike of fault begins to rotate clockwise (Hudnut *et al.*, 2014). The earthquake was well recorded by the strong-motion network operated by the NCEDC, the California Geological Survey and the U.S. Geological Survey (USGS). There are about 12 sites within an epicentral distance of 15 km that had relatively good azimuthal coverage (Fig. 1). The largest peak ground velocity (PGV) of nearly 100 cm/s was observed on station 1765, which is the closest station to the rupture and lies about 3 km east of the northern segment (Fig. 1). The ground deformation associated with the earthquake was also well recorded by the high-resolution COSMO–SkyMed (CSK) satellite and Sentinel-1A satellite, providing independent static observations.

Intriguingly, photos taken at the same location along the southern segment, but at different times, indicate a large amount of afterslip (~20 cm) occurring within the first 24 h following the earthquake (Brooks *et al.*, 2014). Alignment arrays installed after the earthquake by the USGS were able to measure the temporal decay of surface afterslip and also indicate variation of aseismic slip distribution along the fault strike, with the largest afterslip occurring along the southern segment (Lienkaemper *et al.*, 2014). Reports from previous events indicate some temporal afterslip changes (i.e., Hsu *et al.*, 2002, 2006; Freed, 2007) yet lack complete spatial coverage and cross dataset verification. The high-quality datasets for the South Napa earthquake provide a detailed picture of both the spatial and temporal distribution of afterslip and help to distinguish the relative contributions of coseismic and postseismic slip in the observed Interferometric Synthetic Aperture Radar (InSAR) and Global Positioning System (GPS) data.

Our analysis begins with a relocation of the mainshock epicenter, which is done to help constrain the fault location and geometry. Then, to obtain the coseismic slip distribution we rely on the strong-motion waveform data, because they are located close to the fault and provide the best resolution in resolving the rupture details. Although there are also some high-rate GPS sites in the vicinity of the rupture, these data were not fully processed at the time of our work and thus were not included in the current analysis. Once a reliable coseismic slip distribution is obtained, we compare this with the static-only slip model derived from InSAR and GPS data, which includes contributions from both coseismic and postseismic slip and thus allows us to identify potential afterslip regions. These results, combined with the postseismic deformation recorded by the alignment array, are then used to guide dynamic afterslip modeling, which provides insights on the frictional properties along the fault.

EPICENTER RELOCATION

Before performing finite-fault modeling for the mainshock, we refined the epicenter reported by the NCEDC, which usually has uncertainty of a few kilometers because of the need for rapid reporting. Such accuracy is not sufficient for our purpose, because the strong-motion stations are quite close to the

doi: 10.1785/0220140249

epicenter, a few kilometers change of the epicenter could have a large impact on modeling the high-frequency waveform. In addition, a more accurate epicenter will be essential in determining the fault geometry (i.e., dipping direction of the fault), given the well mapped, much higher-resolution surface ruptures. To do this, a single 1D velocity model may not be adequate in the complicated geological settings near the South Napa earthquake (Fig. 1). Thus, we extract site-specific 1D profiles from the 08.3.0 3D Bay area velocity model (Aagaard *et al.*, 2010) to approximate the paths from the hypocenter to each of the various near-fault stations (Fig. 2a). Because the hypocenter is quite deep (11 km) and stations are very close (< 15 km), direct arrival times are mainly controlled by the structure beneath the station, thus such an approximation should be sufficient. To minimize the effect of uncertainties in the 3D velocity model, we will focus on the closest stations again because the ray paths are nearly vertical and the cumulative effect from the error in the 3D velocity model should be the smallest.

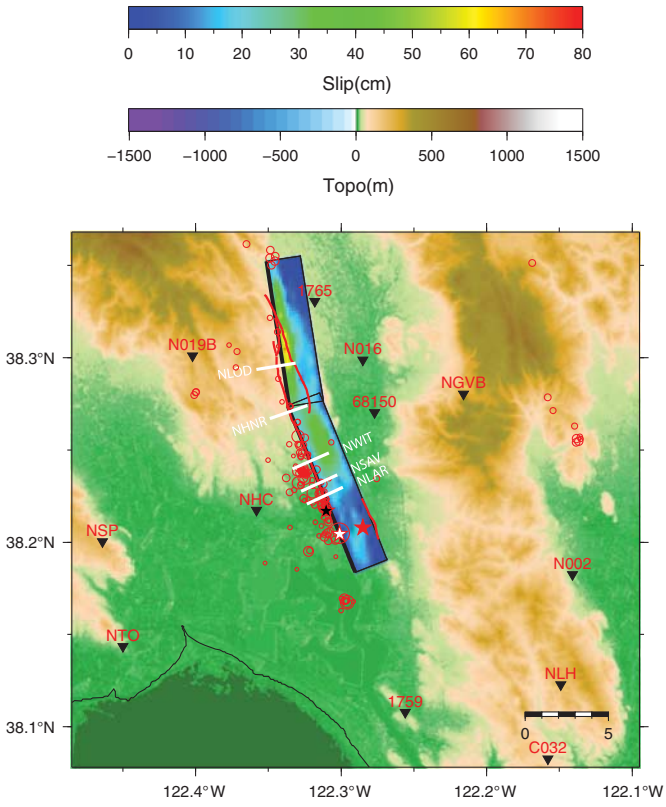

▲ **Figure 1.** Overview of the South Napa earthquake. Map view of the fault segments (rectangles) that are used in the slip inversion of the earthquake: the upper bound of the fault is indicating by heavy solid lines. The strike of the fault segment is chosen based on matching the surface rupture trace (red lines). Strong-motion stations used in this study are indicated by the triangles. The alignment arrays are indicated as white lines (along with their names). The black and red stars show the Northern California Earthquake Data Center (NCEDC) and relocated epicenter location of the mainshock, respectively. The double-difference mainshock relocation from Hardebeck and Shelly (2014) is shown as a white star, and their relocated seismicity in the first week is shown as open red circles, with events of **M** >3.5 indicated as filled circles.

Following this criterion, we select four stations that have the shortest distance given the 1D initial location and use their *P*-wave first arrivals to perform the relocation. Signal-to-noise ratios on these stations are quite high, enabling very accurate first arrival picks (error < 0.01 s), with an example given in Figure 2c. Also note the first arrival on station 68150 is about 0.02 s earlier than that on the station NHC. Assuming the initial NCEDC epicenter predicts a much earlier arrival at NHC than 68150 (red marks in Fig. 2c), given the specified 1D profiles for each station. In fact, using these velocity profiles, any epicenter to the west of the surface rupture trace will predict an earlier arrival at station NHC than at 68150. Thus, these stations provide a strong constraint for the epicenter. The formal relocation was done using a grid search around the initial NCEDC location with grid spacing of 0.002° (~200 m) in longitude and latitude. The search result converges to a location (122.285° W, 38.208° N) about 2 km southeast of the initial location and slightly east of the main surface rupture traces (Fig. 2b), with a 0.3788 s correction for the origin time (24 August 2014 at 10:20:44.03 + 0.3788 s UTC).

We note the mainshock and aftershock epicenters determined by double-difference relocation (Hardebeck and Shelley, 2014; Brocher *et al.*, 2015) lie beneath or slightly west of our fault planes (Fig. 1). Unfortunately, the aftershocks were too small to trigger the strong-motion recorders, so we could not employ a similar relocation analysis for these events as we did for the mainshock. In any case, as discussed further below and in the Ⓔ electronic supplement to this article, the ~2 km uncertainty in mainshock epicenter has little impact on the rupture inversion results.

KINEMATIC RUPTURE INVERSION

To perform kinematic slip modeling, we assume rectangular fault planes, which are divided into smaller subfaults with along-strike and down-dip dimensions of 1 km × 1 km, respectively. Assuming our relocated epicenter, we use two fault segments dipping steeply to the northeast to fit the upper edge of the segments with the well-defined surface rupture traces. The strike of first segment (segment S1) determined in this way is 338°, and the second segment (segment S2) is 351°. The dip of segment S1, in which the hypocenter is located, is 82°, and we assume segment S2 has the same dip angle as segment S1. The inversion method used here is summarized in (Ji *et al.*, 2002), which adopts a simulated annealing method to simultaneously invert the slip, rake, rise time, and average rupture speed on each subfault. Green's functions were computed with a frequency–wavenumber integral method (Zhu and Rivera, 2002) using a 1D velocity model determined as an average of the 3D velocity model near the epicenter. In a series of trial-and-error tests, we found this 1D velocity model is a good approximation for most of the stations except NHC. Thus, we generated another Green's function library for NHC with a 1D velocity profile extracted from the 3D velocity model at the location of NHC,

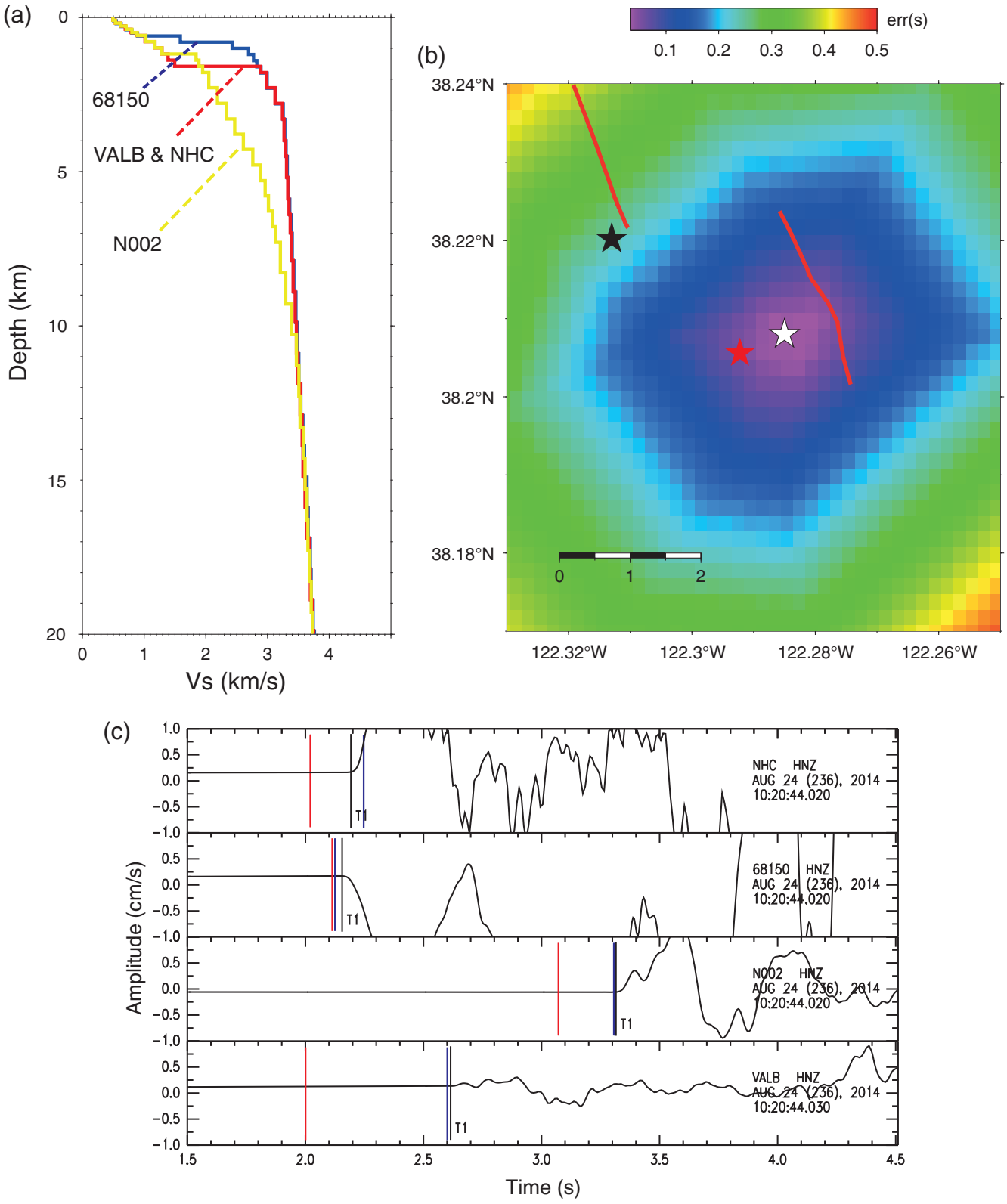

▲ **Figure 2.** Epicenter relocation. (a) 1D profiles extracted from the 3D velocity model, at the location of the four stations. (b) Grid-search results for the epicenter location using the four closest stations. The relocated and NCEDC locations are indicated by a white star and black star, respectively. For comparison, the red star is the relocation obtained when all stations within 15 km are used. (c) First arrival *P*-wave picks (black lines) for the four closest strong-motion stations (NHC, 68150, N002, and VALB); note the slightly earlier arrival on station 68150 compared with NHC. The red lines mark the theoretical arrival time, assuming the original hypocenter location and origin time, and the blue lines are for the relocated hypocenter and new origin time.

although this did not significantly improve the fit for the waveforms at this site.

During the inversion, we let the slip vary from 0 to 200 cm (in intervals of 5 cm), the rise time to change from 0.04 to 1.0 s, and the rupture velocity to range from 2.5 to 3.5 km/s. Our best fits are obtained for a rupture speed around 3.0 km/s, with the fits deteriorating somewhat for faster or slower values. Three-component ground velocity data from 12 sites (Fig. 1) are used in the inversion. We filtered the waveforms to a bandwidth of $f < 3$ Hz for both synthetics and data, and the data and synthetics were aligned on the *P*-wave arrival times during the inversion process. We noted that the vertical components always have the largest waveform misfits; this is mainly due to the 3D velocity structure that cannot be represented in our 1D models, which will be discussed later (Ⓔ see more in the electronic supplement text and Figs. S1, S2). Thus, we down weighted the vertical components by a factor of 2 in the inversion.

Our preferred coseismic slip model is shown in Figure 3, along with the corresponding waveform fits. The inversion result shows that after a relatively weak initiation at a depth of 11 km, the rupture propagated almost unilaterally along strike toward the northwest. There is also significant up-dip rupture directivity, because the strongest asperity (located toward the northern end of the fault) has a centroid depth of only about 3 km. Ⓔ The slip model is characterized by two asperities with one located on segment S1 at deeper depth and one located on S2 with shallower depth, corresponding to the two peaks in the moment-rate function, respectively (Fig. 3). The inverted rupture fits the horizontal components (mainly *S* waves) reasonably well for most of the near-fault sites. Although we have filtered the motions to $f < 3$ Hz, the dominant frequency in the waveforms is around 1 Hz, especially at the stations with large PGVs (i.e., 1765, NHC, 68150, and N016). The stations located to the south (i.e., 1759, NLH, C032, and N002) have smaller PGVs, and their waveforms contain higher-frequency motions compared with other stations.

This feature can be explained by a depth-dependent rise time in our rupture model, in which the average rise time for

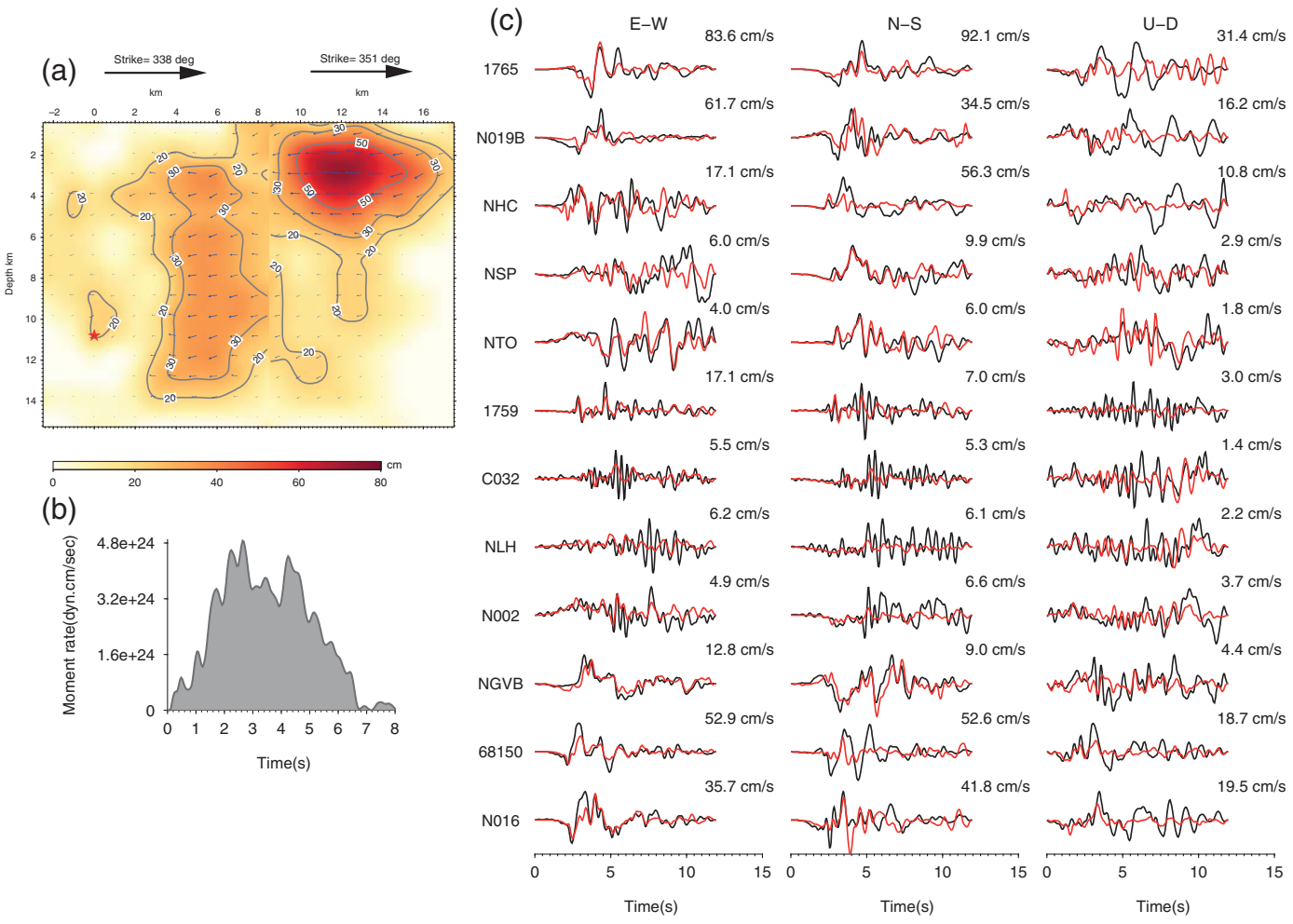

▲ **Figure 3.** Coseismic slip model and waveform fits. (a) Depth profile of slip distribution derived from strong-motion inversion. The red star indicates the hypocenter, and arrows show the rake angles. (b) Moment-rate function for the coseismic slip model. (c) Strong-motion waveform fits for the preferred slip model. Both data and synthetics are shown as velocities and filtered to 3 Hz and lower frequency ranges; the data are in black and synthetics are in red. The station names are shown at the beginning for each station, and the peak amplitude of data is indicated at the end of each trace. (E-W, east–west; N-S; north–south; U-D, up–down)

the shallower (< 5 km) asperity is about 0.2 s longer than the deeper rupture (Fig. 4a). We decomposed contributions to the rupture from depths deeper and shallower than 5 km for stations 1765 and 1759, which are the stations toward and away from the rupture, respectively. As shown in Figure 4b, for station 1765 the *S*-waves energy is mainly coming from the shallow rupture, whereas the opposite is true for station 1759. Thus, it appears the largest ground motions mainly originated from the shallow asperity with longer rise time, and the higher-frequency radiation was mainly coming from deeper rupture having a shorter rise time. Such a depth dependence of rise time has been reported previously by Kagawa *et al.* (2004) and is also well documented for the largest events of the 2012 Brawley swarm in the Imperial Valley (Wei *et al.*, 2013). The lengthening of rise time along the shallow portion of the fault likely results from the rupture propagating into the shallow velocity-strengthening region in surface-rupturing events (e.g., Marone and Scholz, 1988; Dalguer *et al.*, 2008; Pitarka *et al.*, 2009). This feature is also a key component of the simulation methodology proposed by Graves and Pitarka (2010, 2014), who found it helps explain the relative reduction of higher-frequency radiation in surface-rupturing earthquakes.

We also tested the sensitivity of finite-fault inversion to the effect of 3D velocity structure and hypocenter location (Ⓔ see the 3D Modeling Description section and Sensitivity Test of Segment S1 Dip section in the electronic supplement). We find that although using the 3D model increases the amplitudes on the vertical components by roughly a factor of 2, it does not greatly improve the fit to the horizontal motions (Ⓔ Figs. S1, S2). In the future, once the 3D model has been more fully validated using smaller events, 3D Green's functions can be used for the rupture inversion. Ⓔ In addition, our results indicate the kinematic inversion is not that sensitive to small perturbations in the location and geometry of segment S1, because most of the coseismic slip is located on S2 (Fig. S3). Clearly, segment S1 is near vertical; however, based on the inversion alone we cannot distinguish between a slight inclination to the southwest versus a slight inclination to the northeast. Our choice to use a dip to the northeast is constrained solely by our relocated mainshock epicenter.

STATIC SLIP INVERSION

We derived the static slip model by inverting the InSAR data that recorded the ground deformation associated with the earthquake. We used the CSK data from the Italian Space Agency (acquired on 26 July and 27 August 2014) and the Sentinel-1A (S1A) data from European Space Agency (acquired on 7 and 31 August 2014) to map the surface displacement. Both CSK and S1A interferograms are from descending tracks (satellite travelling south) and measure ground displacement in their radar line-of-sight directions, which are about 29° and 23° from the vertical with a component toward the east, respectively. We used a quadtree scheme to subsample the interferograms to 682 data points for the CSK interferogram and 382 data points for the S1A interferogram (Jonsson *et al.*, 2002). The quadtree structure is based on the displacement gradient predicted from the initial strong-motion source model and surface offset observations, ensuring more points near the ruptures.

To verify the fault geometry used in seismic inversion, we tried an inversion with fault segments dipping to the southwest and found that the misfit is slightly larger than that for the

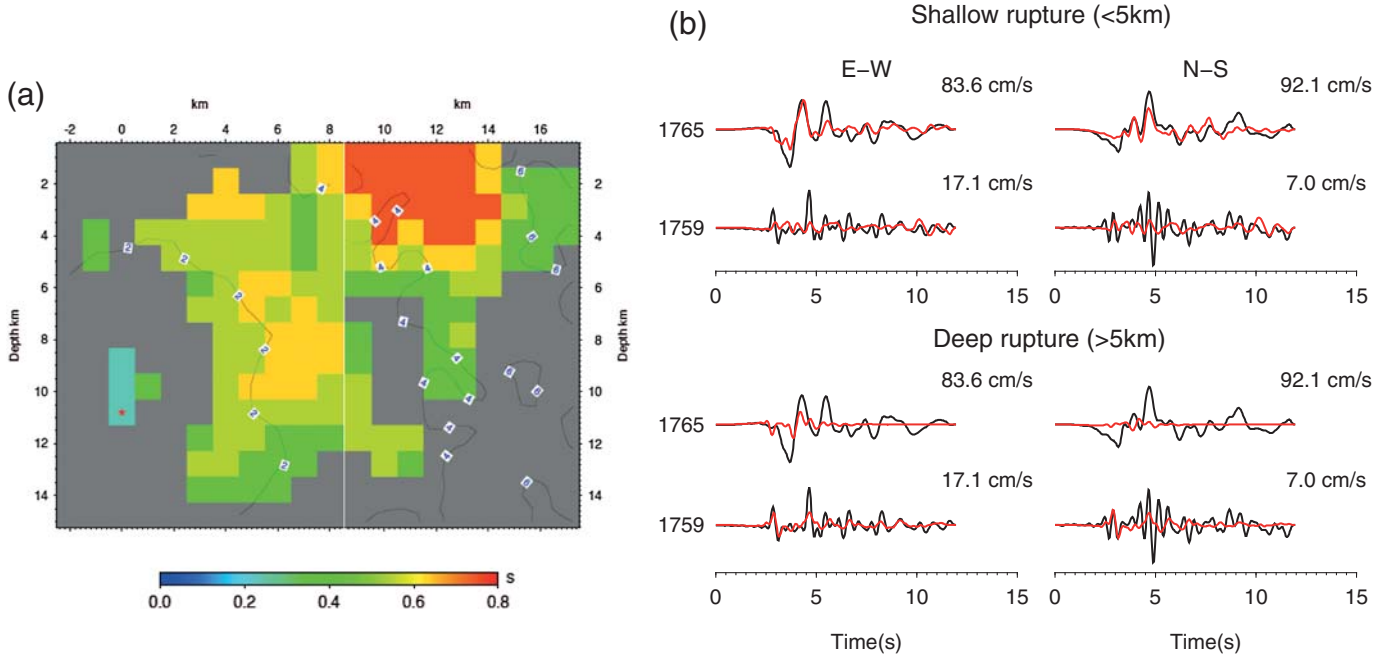

▲ **Figure 4.** Rise time and frequency content analysis. (a) Depth profile of smoothed rise time distribution. (b) Waveform decomposition for station 1765 and 1759, for the contribution from deep rupture (>5 km) and shallow rupture (<5 km).

northeast-dipping faults, thus we assume the same fault geometry as we used in seismic waveform inversions. Our preferred static slip model is shown in Figure 5a, along with the fits to the data (Fig. 5b). In general, our inverted static slip model can fit the InSAR data pretty well. This model also does reasonably well in fitting the static GPS offsets determined from differencing observations one day before and one day after the earthquake (Fig. 5c). It is quite clear that the static slip model has two major asperities, with one located on each of the two fault segments. The asperity on segment S2 (further away from the hypocenter) has very similar location and depth to those of the seismic-only slip model. On the other hand, the asperity on segment S1 has larger slip amplitude and is concentrated at shallower depth compared with the slip distribution obtained in the seismic-only inversion (Fig. 5a). Some of this difference is likely related to the decrease of resolution with increasing depth in the static inversion. Thus, much of the deeper (> 8 km) slip on segment S1 in the coseismic model may be concentrated within the upper few kilometers of the static slip model. However, we also know that large amplitude creep was observed on segment S1 (Lienkaemper *et al.*, 2014), and this postseismic deformation signal should be contained within the time window of the InSAR observations. The contribution of this postseismic afterslip offers an additional explanation of the difference between the static and strong-motion-derived slip models, particularly along the shallowest portion (< 2 km) of segment S1 where the coseismic model has very little slip.

AFTERSLIP MODELING

The deformation that followed the 2014 M_w 6.1 South Napa earthquake was recorded by a wealth of instruments, including GPS and alignment arrays. GPS data from the Plate Boundary Observatory provide us with times series of displacements before, during, and after the earthquake. The closest stations from the ruptured fault are P261, P264, P198, P199, P200, and P202, but they are not closer than 10 km from the epicenter (Fig. 5c). The static offsets on these sites derived from the

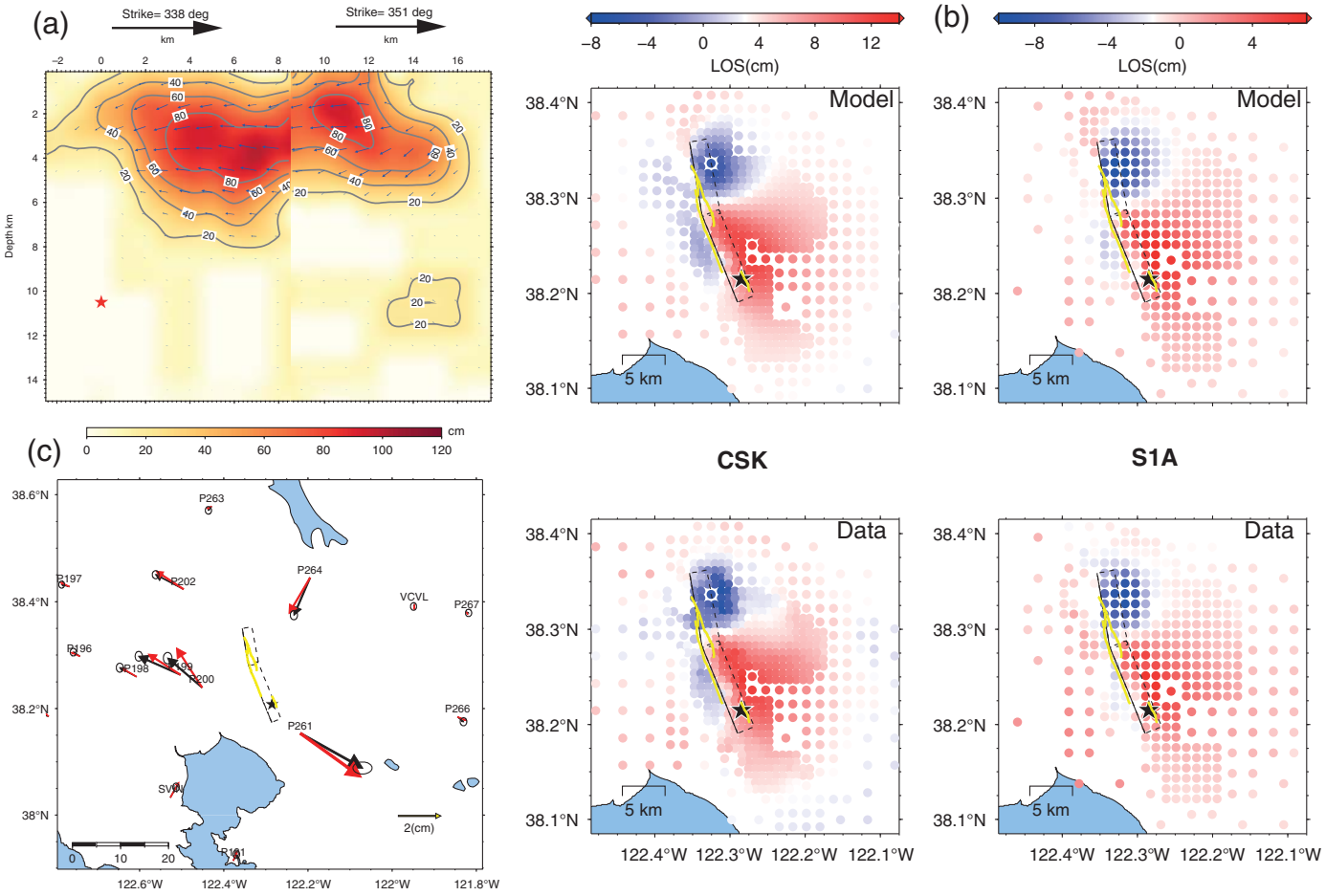

▲ **Figure 5.** Static slip model and static fits. (a) Depth profile of slip distribution derived from inverting Interferometric Synthetic Aperture Radar (InSAR) data. (b) Fits for the down-sampled InSAR data; the data are shown on the bottom and and models are shown on the top. (c) Prediction for the closest horizontal observed GPS offsets (black arrows with errors) using the slip model derived from InSAR data. The GPS offsets were derived from the difference between time series one day before and one day after the earthquake. The contribution of late afterslip (>1 day) is very small at these sites (Ⓔ Fig. S4a). Additional comparisons for the coseismic slip model and coseismic plus three days afterslip can be found in Ⓔ Figure S4b.

difference between time series observed one day before with those from one day and three days after the earthquake shows negligible difference (Ⓔ Fig. S4a), indicating the afterslip more than one day after the earthquake is very small and/or the afterslip is very shallow and localized so that the signals cannot be seen on these stations. At the time of this writing, only a few months of GPS time series are available, and they show at most 5 mm of postseismic displacement, a value commensurate with the typical noise of horizontal GPS data. In sharp contrast, the alignment array data collected by USGS provide us with *in situ* displacement time series at five locations along the fault (Fig. 6a). These measurements indicate up to 25 cm of afterslip just 10 days after the mainshock, illustrating the importance of near-field data to constrain the slip evolution.

Figure 6 also compares the alignment array observations with the coseismic slip model and static slip model. The large shallow slip patch on segment S2 is well resolved in both the coseismic and static slip inversions and is also consistent with the location of maximum surface offset indicated in Figure 6a. On the other hand, we can see a significant difference between the two inverted slip models on segment S1, with the static slip inversion producing much larger shallow slip than is found in the coseismic slip model. As mentioned earlier, part of this is due to the decreasing resolution with depth in the static inversion, which can explain the difference in the deeper portion (>8 km) of the models. However, the static inversion also has 20–30 cm of slip right at the surface along segment S1, which is consistent with the alignment array data and is also required to fit the sharp discontinuity in the InSAR data across the fault trace (Fig. 5b). In contrast, the coseismic slip model has very little surface slip along segment S1. We attribute this difference in the slip models along the shallowest portion of segment S1 to the contribution of rapid afterslip to the InSAR data.

We can also use the alignment data to better understand the dynamics of fault slip and the spatiotemporal relationship between coseismic slip and afterslip on this fault. Surface slip measurements are most sensitive to shallow fault displacements, so they are insufficient to recover the details of the afterslip distribution at depth. This limitation precludes using kinematic inversions to investigate afterslip. As a workaround, we use forward models of stress-driven afterslip to establish whether the near-field observations are compatible with the predictions of a rate-and-state friction model. Stress-driven models are simply forward models of afterslip based on coseismic stress change and rheological assumptions about fault friction. This approach is inspired from the study of the 2004 M_w 6.0 Parkfield earthquake, for which all the geodetic data can be explained by a single dynamic model of slip evolution (Barbot *et al.*, 2012). We assume that afterslip is driven by the coseismic stress change and that only the areas of positive (i.e., right-lateral) stress change develop afterslip (Barbot *et al.*, 2009). To carry out these simulations, we employ Unicycle, an earthquake-cycle simulation code developed at the Earth Observatory of Singapore that resolves all stages of the earthquake cycle with the radiation damping approximation. The approach is similar to that described by

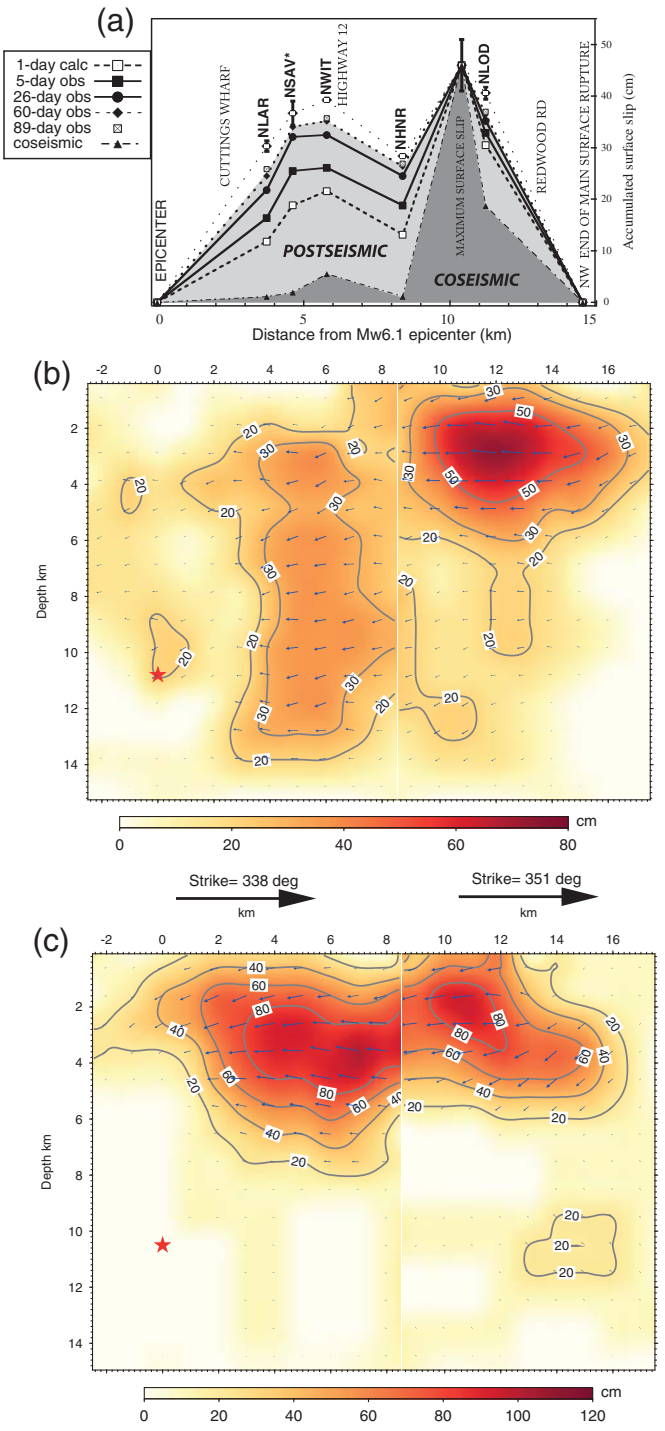

▲ **Figure 6.** Comparison of slip models and the alignment data. The depth profiles of (middle) coseismic and (bottom) static slip models are shown with the (top) afterslip observations obtained by alignment array (Lienkaemper *et al.*, 2014). The name of the alignment station is shown at the top.

other authors (e.g., Perfettini and Avouac, 2004; Johnson *et al.*, 2006; Hetland and Simons, 2010; Kame *et al.*, 2013).

Stress-driven simulations of afterslip produce time series of fault slip, which can be used to predict surface displacements. At a particular fault location, the asymptotic value of afterslip

depends mostly on the coseismic stress change at that point. This can be understood from the relationship between slip and stress for an isolated patch

$$\tau = CG\frac{S}{L}$$

(Kanamori and Anderson, 1975), in which (in this context) τ is the coseismic stress change, S is the amplitude of afterslip, G is the rigidity of rocks, L is the size of the asperity, and C is a constant describing the effect of geometry. More afterslip is obtained for more coseismic stress change. In addition to the asymptotic value of afterslip, these simulations provide us with the time evolution of afterslip. The time dependence of afterslip is controlled by the frictional properties (e.g., Barbot *et al.*, 2009). For aseismic processes, the shape of the relaxation curve and the time scale of the afterslip transient are both controlled by V_0, the characteristic velocity, and the product (a–b) σ, in which a and b are frictional parameters and σ is the effective confining pressure. In general, nontrivial values of V_0 and (a–b) σ do not change the asymptotic value of afterslip. For this reason, it is not always possible to explain postseismic deformation with stress-driven models. For such a model to reproduce surface observations, both the coseismic stress change and the frictional properties must be compatible.

The coseismic slip distribution obtained from our inversion of seismic data is not particularly sensitive to the distribution of shallow slip. This implies the coseismic stress at shallow depth is greatly affected by the parameterization of the inversion procedure, that is, by smoothing and overall discretization of the fault. To mitigate this problem, we constrain the top patches of the coseismic slip distribution with the alignment arrays data such that there is almost no slip on the southern segment and a peak surface slip of 46 cm in the middle of the northern segment. Because high coseismic slip patches are associated with negative stress change, these areas will experience little to no afterslip. For the afterslip simulation, we assume uniform frictional properties on those areas of the fault experiencing positive coseismic stress change. We set $V_0 = 25$ m/yr, and compute results for (a–b) $\sigma = 1.5$, 2, and 4 MPa. Figure 7 compares our simulated results with the alignment array observations. As noted above, the variation in choice of frictional parameters only affects the results at short-time scales, and all of the values examined in this simple model do well in fitting the alignment

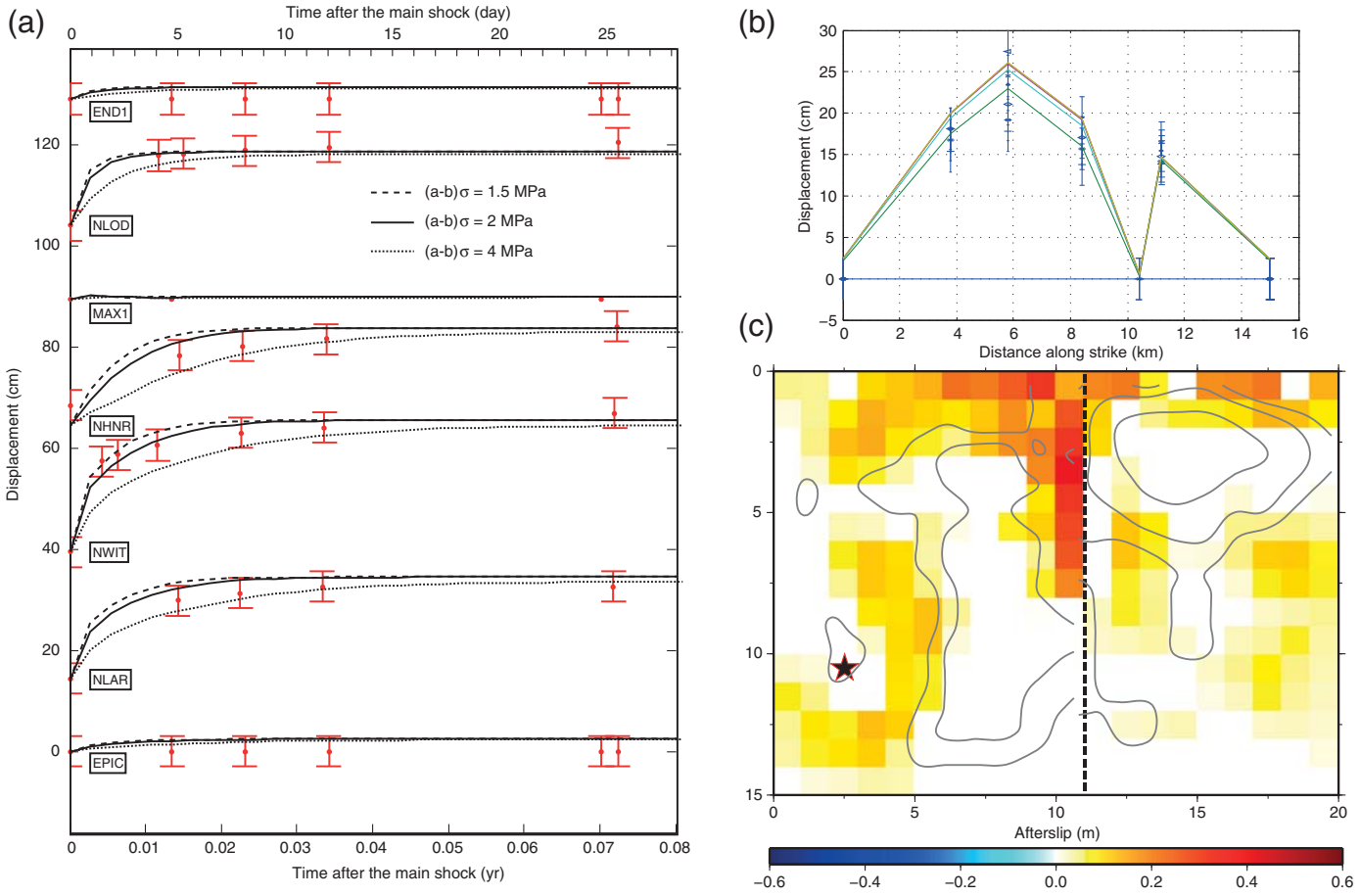

▲ **Figure 7.** Afterslip modeling results. (a) Temporal fits for each of the alignment stations, see Figure 6 for the location of these stations. (b) Along-strike view of the fit to the alignment data. (c) Depth profile of the afterslip; the dashed line indicates the boundary of two fault segments. The gray lines are contours of slip (0.15 m) for the coseismic slip model.

data time series (Fig. 7), with no other optimization required to explain the data. In this model, the cumulative afterslip is mainly concentrated on segment S1 near the surface and is much less significant on segment S2, consistent with the alignment array observations. There is also some afterslip at the junction of segments S1 and S2, which is discussed in the next section. Combining the early afterslip estimated here with the coseismic slip can explain the static GPS offsets as well as the InSAR slip model, given the current level of uncertainties in these measurements (Ⓔ Fig. S4b).

DISCUSSION

The rapid and large afterslip observed for the South Napa earthquake raises an important issue in joint inversion of finite-slip models using multiple datasets. Because the InSAR images were derived from observations obtained a few days after the earthquake, these data include both coseismic and any rapid postseismic deformation. A joint inversion with such data and seismic waveform data can give a misleading result. This also raises possible concerns with the joint inversions for historical events, in which quantitative afterslip observations were either not made or were unavailable. To better understand faulting behavior associated with an earthquake, careful analysis should be conducted for each dataset before considering a joint inversion. Our results for the South Napa earthquake indicate the large differences between the seismic-only and static-only slip inversions can be largely explained by afterslip.

The hypocenter of the earthquake was located at a depth much greater than the major asperities in an area of relatively minor slip, supporting the hypothesis that the nucleation point is often located in regions of low coseismic slip. One hypothesis is that hypocenters of large earthquakes could systematically be located at the edges of creeping zones, which are manifested in the finite-source slip maps as zones of low slip. Because most South Napa aftershocks are located at a deeper,7 ~ 12 km range (Hardebeck and Shelly, 2014; Brocher *et al.*, 2015), such observations of small-scale seismicity can be seen as the boundary between locked zones and actively creeping regions on the fault plane (Rubin *et al.*, 1999; Schaff *et al.*, 2002; Waldhauser and Ellsworth, 2002). The rise time for the slip deeper than 5 km is systematically shorter than that at shallower depth, which is consistent with frequently occurring smaller events. The shallow asperity has the largest coseismic slip and is characterized by longer rise time and a lack of aftershocks, implying that this shallow asperity is likely triggered by dynamic processes during the earthquake rupture. Because earthquakes, whether mainshock or aftershocks, rarely nucleate at such shallow depth, the shallow fault zone is probably in a conditional stable or slip/rate strengthening status. Furthermore, the aftershock distribution does not show clear delineation of the fault geometry, even after relocation (Hardebeck and Shelly, 2014; Brocher *et al.*, 2015), suggesting the possibility that these events may not be on the main fault trace. The cause for such spatial and temporal distribution of the aftershocks is still an open question.

Both the alignment array data and the stress-driven afterslip simulation indicate that most of the shallow afterslip occurs within a few days of the mainshock. This is compatible with the idea that the relaxation time of small fault areas is shorter than that for larger fault domains, everything else being the same (Barbot *et al.*, 2009). In the South Napa earthquake, the coseismic rupture reached shallower depths than are typical for other strike-slip earthquakes (Fialko *et al.*, 2005). For example, most of the coseismic slip of the similar-sized 2004 M_w 6.0 Parkfeld earthquake was confined in the 7–11 km depth range. This leaves a smaller width of fault available for afterslip, leading to a more rapid transient afterslip. The afterslip simulation also indicates that significant afterslip can be expected at the transition of the two fault segments (i.e., near array NHNR), separating the two peaks in the coseismic moment-rate function (Fig. 7c). This prediction is the result of the large positive coseismic stress change at this location. It is possible that this barrier is a permanent feature and a constant obstacle to rupture propagation (e.g., Kaneko *et al.*, 2010). Together, the seismic data, the alignment array, and the stress-driven simulations of afterslip indicate that the coseismic slip was deeper and of less amplitude on the southern segment and shallower than expected in the northern segment. The large slip at shallow depth may be due to different frictional properties at the depth due to the fault penetrating different host rocks. Or the unusual slip distribution can be the result of complex rupture dynamics in a highly heterogeneous fault with multiple barriers and structural changes.

CONCLUSION

In summary, our analysis of the M_w 6.1 South Napa earthquake indicates the rupture occurred on two near-vertical fault segments, each dipping about 82° to the northeast. The northeast dip of the southernmost fault segment is consistent with our relocation of the mainshock epicenter and the mapped surface rupture, although our inversion cannot rule out a vertical or slight dip to the southwest for this segment. Our strong-motion inversion result indicates the rupture propagated unilaterally to the northwest and most of the coseismic slip occurred along the shallow portion of the northern fault segment about 10 km along strike from the epicenter. Relatively little slip occurred in the hypocentral region of the fault. Our static slip inversion using InSAR data shows two strong asperities located along the shallow portion of each fault segment, corresponding to two peaks in the moment-rate function. The northern asperity is consistent with the location and strength of that determined in our strong-motion inversion; however, the shallowest portion of the southern asperity is located in a region having relatively little coseismic slip in the strong-motion model. This apparent discrepancy is resolved by accounting for the contribution of afterslip in the static inversion model and is supported by alignment array observations, which indicate substantial postseismic deformation occurred along the southern fault segment following the mainshock rupture.

ACKNOWLEDGMENTS

Strong-motion waveform data was downloaded from the Northern California Data Center, California Geological Survey, and U.S. Geological Survey (USGS) (strongmotioncenter.org; last accessed September 2014). Interferometric Synthetic Aperture Radar data were obtained from the Jet Propulsion Laboratory (JPL), static GPS data were made available by Tom Herring from the Massachusetts Institute of Technology. Constructive reviews by Annemarie Baltay, Art Frankel, and an anonymous reviewer led to improvements in the manuscript. Figures were made using Generic Mapping Tool (Wessel and Smith, 1991). Part of this research was carried out at JPL (California Institute of Technology), sponsored by the National Aeronautics and Space Administration.

REFERENCES

Aagaard, B. T., R. W. Graves, A. Rodgers, T. M. Brocher, R. W. Simpson, D. Dreger, N. A. Petersson, S. C. Larsen, S. Ma, and R. C. Jachens (2010). Ground-motion modeling of Hayward fault scenario earthquakes, Part II: Simulation of long-period and broadband ground motions, *Bull. Seismol. Soc. Am.* **100,** no. 6, 2945–2977.

Barbot, S., Y. Fialko, and Y. Bock (2009). Postseismic deformation due to the M_w 6.0 2004 Parkfield earthquake: Stress-driven creep on a fault with spatially variable rate-and-state friction parameters, *J. Geophys. Res.* **114,** doi: 10.1029/2008JB005748.

Barbot, S., N. Lapusta, and J. P. Avouac (2012). Under the hood of the earthquake machine: Toward predictive modeling of the seismic cycle, *Science* **336,** no. 6082, 707–710.

Brocher, T. A., A. Baltay, J. L. Hardebeck, J. Polet, E. Langenheim, A. L. Llenos, J. J. Lienkaemper, D. P. Schwartz, J. L. Blair, T. Dawson, *et al.* (2015). The **M** 6.0 24 August 2014 South Napa earthquake, *Seismol. Res. Lett.* **86,** no. 2A, doi: 10.1785/0220150004.

Brooks, B., K. Hudnut, C. Glennie, and T. Ericksen (2014). Near-field deformation associated with the **M** 6.0 South Napa earthquake surface rupture, in *2014 Fall Meeting, AGU*, San Francisco, California, 14–19 December 2014, Abstract S33F-4900.

Dalguer, L. A., H. Miyake, S. M. Day, and K. Irikura (2008). Surface rupturing and buried dynamic-rupture models calibrated with statistical observations of past earthquakes, *Bull. Seismol. Soc. Am.* **98,** no. 3, 1147–1161.

Fialko, Y., D. Sandwell, M. Simons, and P. Rosen (2005). Three-dimensional deformation caused by the Bam, Iran, earthquake and the origin of shallow slip deficit, *Nature* **435,** no. 7040, 295–299.

Freed, A. M. (2007). Afterslip (and only afterslip) following the 2004 Parkfield, California, earthquake, *Geophys. Res. Lett.* **34,** no. 6, doi: 10.1029/2006GL029155.

Graves, R. W., and A. Pitarka (2010). Broadband ground-motion simulation using a hybrid approach, *Bull. Seismol. Soc. Am.* **100,** no. 5A, 2095–2123.

Graves, R., and A. Pitarka (2014). Refinements to the Graves and Pitarka (2010) ground-motion simulation method, *Seismol. Res. Lett.* **86,** no. 1, 75–80, doi: 10.1785/0220140101.

Hardebeck, J. L., and D. Shelly (2014). Aftershocks of the 2014 **M** 6 South Napa Earthquake: Detection, location, and focal mechanisms, in *2014 Fall Meeting, AGU*, San Francisco, California, 14–19 December 2014, Abstract S33F-4927.

Hetland, E. A., and M. Simons (2010). Post-seismic and interseismic fault creep II: Transient creep and interseismic stress shadows on megathrusts, *Geophys. J. Int.* **181,** no. 1, 99–112.

Hsu, Y. J., N. Bechor, P. Segall, S. B. Yu, L. C. Kuo, and K. F. Ma (2002). Rapid afterslip following the 1999 Chi-Chi, Taiwan earthquake, *Geophys. Res. Lett.* **29,** no. 16, doi: 10.1029/2002GL014967.

Hsu, Y. J., M. Simons, J. P. Avouac, J. Galetzka, K. Sieh, M. Chlieh, D. Natawidjaja, L. Prawirodirdjo, and Y. Bock (2006). Frictional afterslip following the 2005 Nias-Simeulue earthquake, Sumatra, *Science* **312,** no. 5782, 1921–1926.

Hudnut, K., C. Glennie, B. Brooks, D. Hauser, T. Ericksen, J. Boatwright, A. Rosinski, T. Dawson, T. Mccrink, and D. Mardock, et al. (2014). Near-field deformation associated with the South Napa earthquake (**M** 6.0) using differential airborne LiDAR, in *2014 Fall Meeting, AGU*, San Francisco, California, 14–19 December 2014, Abstract S33F-4896.

Ji, C., D. J. Wald, and D. V. Helmberger (2002). Source description of the 1999 Hector Mine, California, earthquake, part I: Wavelet domain inversion theory and resolution analysis, *Bull. Seismol. Soc. Am.* **92,** no. 4, 1192–1207.

Johnson, K. M., R. Burgmann, and K. Larson (2006). Frictional properties on the San Andreas fault near Parkfield, California, inferred from models of afterslip following the 2004 earthquake, *Bull. Seismol. Soc. Am.* **96,** no. 4, S321–S338.

Jonsson, S., H. Zebker, P. Segall, and F. Amelung (2002). Fault slip distribution of the 1999 M_w 7.1 Hector Mine, California, earthquake, estimated from satellite radar and GPS measurements, *Bull. Seismol. Soc. Am.* **92,** no. 4, 1377–1389.

Kagawa, T., K. Irikura, and P. G. Somerville (2004). Differences in ground motion and fault rupture process between the surface and buried rupture earthquakes, *Earth Planets Space* **56,** no. 1, 3–14.

Kame, N., S. Fujita, M. Nakatani, and T. Kusakabe (2013). Earthquake cycle simulation with a revised rate- and state-dependent friction law, *Tectonophysics* **600,** 196–204.

Kanamori, H., and D. L. Anderson (1975). Theoretical basis of some empirical relations in seismology, *Bull. Seismol. Soc. Am.* **65,** no. 5, 1073–1095.

Kaneko, Y., J. P. Avouac, and N. Lapusta (2010). Towards inferring earthquake patterns from geodetic observations of interseismic coupling, *Nat. Geosci.* **3,** no. 5, 363–369.

Lienkaemper, J. J., B. Brooks, S. DeLong, C. Domrose, and C. Rosa (2014) Surface slip associated with the 2014 South Napa, California earthquake measured on alinement arrays, in *2014 Fall Meeting, AGU*, San Francisco, California, 14–19 December 2014, Abstract S33F-4898.

Marone, C., and C. H. Scholz (1988). The depth of seismic faulting and the upper transition from stable to unstable slip regimes, *Geophys. Res. Lett.* **15,** no. 6, 621–624.

Perfettini, H., and J. P. Avouac (2004). Postseismic relaxation driven by brittle creep: A possible mechanism to reconcile geodetic measurements and the decay rate of aftershocks, application to the Chi-Chi earthquake, Taiwan, *J. Geophys. Res.* **109,** no. B2, doi: 10.1029/2003JB002488.

Pitarka, A., L. A. Dalguer, S. M. Day, P. G. Somerville, and K. Dan (2009). Numerical study of ground-motion differences between buried-rupturing and surface-rupturing earthquakes, *Bull. Seismol. Soc. Am.* **99,** no. 3, 1521–1537.

Rubin, A. M., D. Gillard, and J. L. Got (1999). Streaks of microearthquakes along creeping faults, *Nature* **400,** no. 6745, 635–641.

Schaff, D. P., G. H. R. Bokelmann, G. C. Beroza, F. Waldhauser, and W. L. Ellsworth (2002). High-resolution image of Calaveras fault seismicity, *J. Geophys. Res* **107,** no. B9, doi: 10.1029/2001JB000633.

Waldhauser, F., and W. L. Ellsworth (2002). Fault structure and mechanics of the Hayward fault, California, from double-difference earthquake locations, *J. Geophys. Res.* **107,** no. B3, doi: 10.1029/2000JB000084.

Wei, S. J., D. Helmberger, S. Owen, R. W. Graves, K. W. Hudnut, and E. J. Fielding (2013). Complementary slip distributions of the largest earthquakes in the 2012 Brawley swarm, Imperial Valley, California, *Geophys. Res. Lett.* **40,** no. 5, 847–852.

Wessel, P., and W. H. F. Smith (1991). Free software helps map and display data, *Eos Trans. AGU* **72,** 441.

Zhu, L. P., and L. A. Rivera (2002). A note on the dynamic and static displacements from a point source in multilayered media, *Geophys. J. Int.* **148,** no. 3, 619–627.

Shengji Wei[1]
Sylvain Barbot
Earth Observatory of Singapore (EOS)
Nanyang Technological University
50 Nanyang Avenue
Block N2-01a-15
Singapore 639798
Singapore
shjwei@gmail.com

Robert Graves
Kenneth Hudnut
U.S. Geological Survey
525 South Wilson Avenue
Pasadena, California 91106 U.S.A.

James J. Lienkaemper
U.S. Geological Survey
345 Middlefield Road, MS-977
Menlo Park, California 94025 U.S.A.

Teng Wang
King Abdullah University of Science and Technology
4700 King Abdullah University of Science and Technology
Thuwal 23955-6900
Saudi Arabia

Yuning Fu
Jet Propulsion Laboratory
California Institute Technology
4800 Oak Grove Drive
Pasadena, California 91109 U.S.A.

Don Helmberger
California Institute of Technology
Seismological Laboratory
1200 East California Boulevard, MS 252-21
So. Mudd Building, Room 261
Pasadena, California 91125 U.S.A.

[1] Also at Seismological Laboratory, California Institute Technology, 1200 East California Boulevard, MS 252-21, So. Mudd Building, Room 261, Pasadena, California 91125 U.S.A.